Full-field noise-correlation elastography for in-plane mechanical anisotropy imaging

Agathe Marmin, Nina Dufour, Sybille Facca, Stefan Catheline, Simon Chatelin, Amir Nahas

Research Article | Vol. 15, No. 4 / 1 Apr 2024 / Biomedical Optics Express 2622
Biomedical Optics EXPRESS

Full-field noise-correlation elastography for in-plane mechanical anisotropy imaging

AGATHE MARMIN,[1] NINA DUFOUR,[1] SYBILLE FACCA,[1,2] STEFAN CATHELINE,[3] SIMON CHATELIN,[1,4] AND AMIR NAHAS[1,*]

[1]Université de Strasbourg, CNRS, ICube, UMR 7357, 67000 Strasbourg, France
[2]Department of Hand Surgery, SOS hand, University Hospital of Strasbourg, FMTS, 1 avenue Molière, 67000 Strasbourg, France
[3]LabTAU, Inserm, Centre Léon Bérard, Université Lyon 1, Univ Lyon, F-69003 Lyon, France
[4]RoDIn, Inserm ERL1328, 1 place de l'Hôpital, 67000 Strasbourg, France
[*]amir.nahas@unistra.fr

Abstract: Elastography contrast imaging has great potential for the detection and characterization of abnormalities in soft biological tissues to help physicians in diagnosis. Transient shear-waves elastography has notably shown promising results for a range of clinical applications. In biological soft tissues such as muscle, high mechanical anisotropy implies different stiffness estimations depending on the direction of the measurement. In this study, we propose the evolution of a noise-correlation elastography approach for in-plane anisotropy mapping. This method is shown to retrieve anisotropy from simulation images before being validated on agarose anisotropic tissue-mimicking phantoms, and the first results on *in-vivo* biological fibrous tissues are presented.

1. Introduction

A number of pathologies such as malignant tumors, metastasis or inflammatory diseases alter the structure of biological tissues. These changes of structure modify the mechanical properties of tissues and organs. Manual palpation was commonly used for many years by physicians to screen for suspicious abnormalities in patients. Palpation is yet limited to a qualitative assessment of important lesions in accessible tissues. Elastography has emerged as a virtual palpation tool to provide physicians with structural information to help with the diagnosis of lesions. In the last 40 years, imaging tools have been developed to measure mechanical properties of tissues using ultrasounds [1,2] or MRI [3,4]. In 1998, an OCT system was the first optical system reported to perform elastography measurements [5]. Since then, a number of elastography methods have been adapted to optical setups, allowing for real-time and high-resolution imaging [6], which has demonstrated great potential for clinical application, providing quantitative non-contact stiffness measurements [7–9].

Most elastography techniques assume soft biological tissues as isotropic, however the structure of a number of soft tissues makes their mechanical properties dependent on the probing direction. Anisotropic behavior has been shown in a range of tissues such as muscle [10–13], kidney [14], brain tissues [15–17], breast lesions [18], skin [19,20] or cornea [21,22]. In the case of mechanical anisotropy, using elastography methods assuming tissue isotropy can introduce strong bias in stiffness measurements [23]. In order to account for soft biological tissues' anisotropic behavior, different models can be found in literature [24–26]. Among others, the linear transverse isotropic model considers a symmetry axis within the tissue along the fibers' direction to reduce system parameters with reasonable simplifications [27].

Experimental imaging of soft biological tissues' anisotropic mechanical properties have mainly been performed using ultrasound imaging techniques [10,14,19,28–35] or Magnetic Resonance Elastography (MRE) [15–18,36–38]. MRE approaches to anisotropy imaging rely

#516166 https://doi.org/10.1364/BOE.516166
Journal © 2024 Received 5 Jan 2024; revised 4 Mar 2024; accepted 5 Mar 2024; published 26 Mar 2024

Biomedical Optics EXPRESS

generally on the imaging of an harmonic mechanical field in the sample. On the other hand, most ultrasound-based elastography approaches found in literature for anisotropic biological tissues rely on transient elastography. Directional mechanical properties are extracted from the propagation of a mechanical impulse in the sample and successive measurements are acquired with different impulse positions to retrieve information on mechanical anisotropy. Ultrasound approaches based on 4D imaging or specific probes have recently offered a promising solution for clinical imaging to improve repeatability and accuracy of ultrasound shear-wave velocity measurements [32,39,40]. Ultrasound and MRI-based modalities have shown that stiffness anisotropy of gray matter changes with age [16], and allowed for characterization of breast tumors [18,30,31,33,41] or kidney fibrosis [14] but also for diagnostic and clinical treatment of muscle injury or muscle atrophy as a consequence of a pathology [35,42–44].

Optical elastography has been developed to overcome the limitations of MRI and ultrasound imaging in terms of frequency and resolution in small and thin structures [45]. Despite acquisition depths shallower than MRI or ultrasound modalities, optics achieves contactless and real-time imaging at a micrometer-scale, making optical elastography especially well-adapted to skin, eye imaging and endoscopy. Transient optical elastography experimental studies on mechanical anisotropy have been performed recently using a directional shear-wave source and rotating the sample at different angles [20,21,46]. These first studies on anisotropy imaging using optical systems have shown promising results in skin and cornea imaging and demonstrated the possibility to retrieve anisotropy information using transient Optical Coherence Elastography (OCE). Transient OCE approaches based on the sample rotation require increased acquisition times as the propagation of a mechanical impulse through the sample only probes a single direction of propagation at a time. To date, this approach has consequently shown anisotropy measurements but may not be well-adapted for clinical studies. Other OCE approaches for anisotropy imaging have emerged in literature in recent years based on a layered model [47] or on harmonic excitation [48], providing anisotropy measurements in homogeneous *ex-vivo* biological tissues. To our knowledge, transient elastography is yet the most quantitative approaches in optical elastography for clinical translation [6,8,49,50] and is the focus of this paper.

Classical transient OCE typically requires multiple high speed scans to retrieve a stiffness image. To overcome this limitation, a recent method based on diffuse fields intrinsic to *in-vivo* biological tissues has been introduced to optical elastography [48,51,52]. Contrary to classical transient elastography, which is based on a single direction of propagation, with noise-correlation transient elastography, shear-waves are generated in the sample in all directions. When combined with a full-field imaging system, noise-correlation allows to retrieve in-plane stiffness anisotropy images in-real-time without needing to rotate the sample.

We present here elastography combining a full-field digital holography setup with a time-reversal method adapted for fibrous tissue. Considering transverse isotropy in the sample, we demonstrate that the in-plane anisotropy of the medium can be retrieved by analyzing the two-dimensional noise wave-field. Experimental images are presented on tissue-mimicking anisotropic polymer samples. First *in-vivo* anisotropy results are presented on the human forearm.

2. Materials and methods

2.1. Shear-wave propagation in anisotropic biological soft tissues

In order to have a quantitative measurement of the stiffness of soft biological tissues and its in-plane anisotropy, we propose here to exploit the link between the propagation speed of shear-waves in soft biological tissues and the tissue's mechanical properties.

Evaluating the stiffness of soft biomedical tissues can be used as an equivalent of palpation. The shear modulus (μ, the 2^{nd} Lamé's coefficient) is often used for biomedical application.

We consider here an incompressible (Poisson's ratio = 0.5) infinite homogeneous medium. The shear-wave speed (c) in such medium can be link to its shear modulus by the following

Biomedical Optics EXPRESS

formula:

$$\mu = \rho c^2 \tag{1}$$

with ρ the medium's mass density.

In the case of anisotropic soft biological tissues, we assume here a symmetry axis along the direction of the fibers. Under this assumption, the medium can be considered as transverse isotropic [10]. In the anisotropic case, a tensor notation is required to describe the stiffness. The stiffness tensor $\mathbf{C}$ is then defined using the generalized Hook's law as:

$$\sigma = \mathbf{C}\epsilon \tag{2}$$

with ϵ and σ the strain and stress tensors, respectively.

Assuming transverse isotropy, the stiffness tensor can be expressed using Voigt's notation as:

$$\mathbf{C} = \begin{pmatrix} c_{11} & c_{11}-2c_{66} & c_{13} & 0 & 0 & 0 \\ c_{11}-2c_{66} & c_{11} & c_{13} & 0 & 0 & 0 \\ c_{13} & c_{13} & c_{33} & 0 & 0 & 0 \\ 0 & 0 & 0 & c_{44} & 0 & 0 \\ 0 & 0 & 0 & 0 & c_{44} & 0 \\ 0 & 0 & 0 & 0 & 0 & c_{66} \end{pmatrix} \tag{3}$$

We define here the transverse shear-wave speed ($c_\perp$) when the direction of propagation is perpendicular to the fiber's axis and the parallel shear-wave speed ($c_\parallel$) where the direction of propagation is along the fibers. The coefficient of the stiffness matrix can be expressed as [10]:

$$\begin{aligned} c_{44} &= \rho c_\parallel^2 \\ c_{66} &= \rho c_\perp^2 \end{aligned} \tag{4}$$

Consequently, when considering the surface of a transverse isotropic sample, the local stiffness can be described as a function of the angle between the considered direction of stiffness evaluation (θ) and the local main fiber orientation (θ_0).

According to the Christoffel equations, we finally consider the following expression for shear modulus [53]:

$$\mu(\theta) = \rho(c_\perp^2 sin^2(\theta-\theta_0) + c_\parallel^2 cos^2((\theta-\theta_0)) \tag{5}$$

with the density ρ of biological soft tissue assumed to be $1.000 g/cm^3$.

2.2. *Shear-wave directional velocity estimation from the displacement field using two-dimensional noise-correlation*

The principle of noise-correlation elastography is using spatiotemporal correlation to refocus the noise-field and access the local stiffness quantitatively. The combination of full-field quantitative displacement imaging with noise correlation allows for two-dimensional spatiotemporal correlation. In previous studies using both full-field imaging and noise-correlation, isotropic samples with isotropic noise field were considered [52] as well as isotropic samples with spatially-coherent mechanical sources [54]. We propose here to examine the case of transverse isotropic media in the presence of an isotropic noise field.

Biomedical Optics EXPRESS

Noise correlation elastography relies on the link between the correlation C of a noise field Ψ and the Green function (G) at the positions $\overrightarrow{r_0}$ and $\overrightarrow{r}$ as [55]:

$$\frac{\partial}{\partial t}C(\overrightarrow{r_0},\overrightarrow{r},t)\propto Im[G(\overrightarrow{r_0},\overrightarrow{r},t)]\,. \tag{6}$$

Where t is time, Im is the imaginary part and C the correlation function defined as:

$$C(\overrightarrow{r_0},\overrightarrow{r},t) = \Psi(\overrightarrow{r_0},t)\otimes\Psi(\overrightarrow{r},t)\,. \tag{7}$$

Considering a semi-infinite, transversely isotropic, elastic and homogeneous medium, the exact Green function is relatively complex but well described in [56,57]. To simplify the expression of the Green function, we can make the following approximations in this study: shear-wave sources and detectors have the same direction, the waves detected are surface waves, far field approximation for the shear-waves (the sources are far from the detection field of view) and a long exposure time which washes out the compression wave contribution. Using these approximations, the simplify Green function can be written:

$$G(\overrightarrow{r_0}=0,\overrightarrow{r},\omega) = \frac{1}{4\pi\rho c_{66}\sqrt{c_{44}}}e^{i\omega\sqrt{\frac{r_\perp^2}{c_{66}}+\frac{r_\parallel^2}{c_{44}}}}\,. \tag{8}$$

where $r_\perp = \overrightarrow{r}.\overrightarrow{e_\perp}$ and $r_\parallel = \overrightarrow{r}.\overrightarrow{e_\parallel}$ with $\overrightarrow{e_\perp}$ and $\overrightarrow{e_\parallel}$ the direction perpendicular and parallel to the fibers respectively.

Thus, considering an ideal isotropic diffuse field, the shear-wave speeds $c_\perp$ along $\overrightarrow{e_\perp}$ and $c_\parallel$ along $\overrightarrow{e_\parallel}$ can be retrieved using the noise-correlation derivative approach described in [52,55,58]:

$$\begin{cases} c_\perp = \sqrt{\dfrac{c_{66}}{\rho}} = 2\pi f_0\sqrt{-\dfrac{\psi_z^{\mathrm{TR}}}{\xi_{z\perp}^{\mathrm{TR}}}} \\ c_\parallel = \sqrt{\dfrac{c_{44}}{\rho}} = 2\pi f_0\sqrt{-\dfrac{\psi_z^{\mathrm{TR}}}{\xi_{z\parallel}^{\mathrm{TR}}}} \end{cases} \tag{9}$$

with $\xi_{0\perp}^{\mathrm{TR}}$ and $\xi_{0\parallel}^{\mathrm{TR}}$ the second derivatives of the auto-correlation of the displacement field Ψ respectively along $\overrightarrow{e_\perp}$ and $\overrightarrow{e_\parallel}$. And f_0 the central noise frequency.

In this paper, focal spot images are reconstructed using two-dimensional correlations at $\tau = 0$ as a graphic illustration of the medium's anisotropy. The medium's anisotropy is indeed directly illustrated as an asymmetry in the focal spot. By using the full width at half maximum (FWHM), this image can be converted to an ellipse. The direction of its main axis indicates the preferred propagation direction and the ratio between the major and minor axes of the ellipse yields the anisotropy ratio of the medium. A schematic illustrates this 2-dimensional focal spot approach in Fig. 1 on simulated data.

Since the reconstruction of the focal spot for each point of the image is time-consuming and only possible when the noise's central wavelength is smaller than the field of view, a derivative-based approach was implemented to solve this issue. The method used to perform shear-wave elastography using the time-reversal approach with low frame rate scanners is based on the previous Eq. (10).

Two-dimensional spatiotemporal correlations allow to retrieve shear-wave speed for each pixel as a function of the direction of the spatial derivation. In a previous study [54], shear-wave speed was computed using the trace of the Hessian matrix at each pixel thus averaging the azimuth speed values. We propose here to use the eigen values of the Hessian matrix in order to compute the shear-wave speeds in 2 orthogonal in-plane directions. The eigen values give access to the shear-wave speeds values and the eigen vectors provide the corresponding directions (anisotropy direction and its normal). This method is illustrated in Fig. 2.

Biomedical Optics EXPRESS

2.3. Imaging the shear-wave field using full-field digital holography

In this paper, an off-axis interferometer based on a Mach-Zehnder is used to perform anisotropy imaging. This set-up allows for single-shot full-field phase imaging, which is key in the noise-correlation approach. Phase images are indeed directly linked to the displacements within the sample consequently allowing to image shear-wave wavefronts and acquiring phase images in a single shot ensures the two-dimensional spatial correlation in the images.

The presented set-up is illustrated Fig. 3. The light source is a 671 nm continuous single mode LASER (CNI MSL-FN-671-S) with a total power output of 250 mW. A 1440 by 1440 pixels Complementary Metal Oxide Semiconductor (CMOS) camera (Adimec, Q-2HFW, 12μm

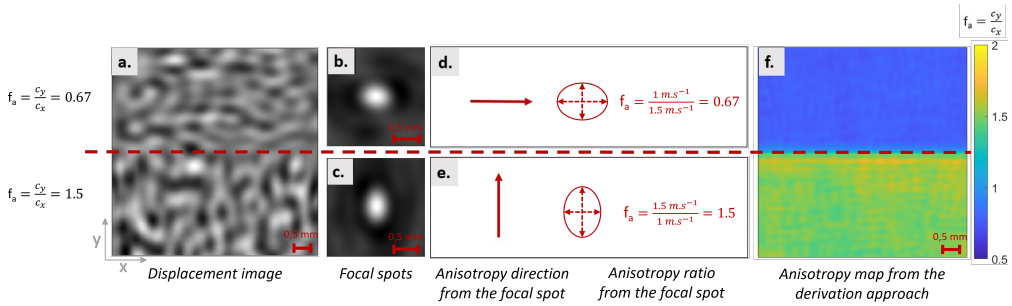

Fig. 1. Illustration of the noise-correlation approach on simulation images with transverse anisotropy. The steps of the focal-spot-width approach are detailed here. (a) is a frame from the simulated movie. On the upper part, the x-axis speed is 1.5 m.s^{-1} and the y-axis speed is 1 m.s^{-1}, corresponding to a 0.67 anisotropy ratio. On the lower part, the x-axis speed is 1 m.s^{-1} and the y-axis speed is 1.5 m.s^{-1}, corresponding to a 1.5 anisotropy ratio. (b) and (c) are focal spots computed for each side, represented by an ellipse in (d) and (e) where the shear-wave speed ratio is computed. (f) is the anisotropy map retrieved from the simulated movie using a derivative approach (Eq. (10)).

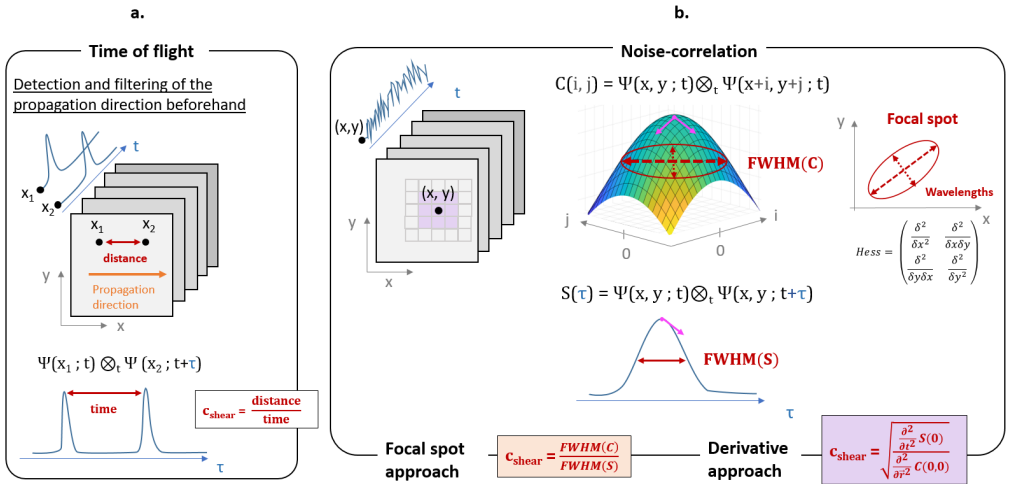

Fig. 2. Illustration of the noise-correlation derivation approach and focal spot approach for anisotropy imaging. (a) represents the classical time-of-flight processing for full-field propagation movies (b) represents the corresponding noise acquisition. The spatial correlation function at t = 0 is noted C and the temporal correlation function is noted S. The derivative and focal spot approaches are illustrated for one point (x,y).

Biomedical Optics EXPRESS

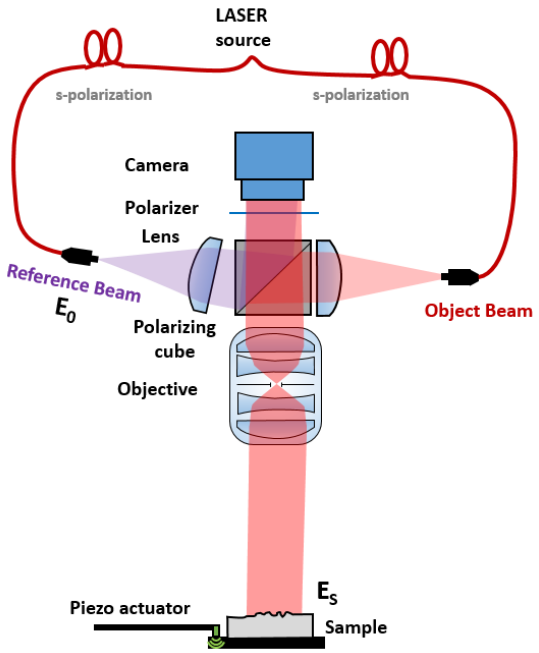

Fig. 3. Schematic of the compact holographic off-axis setup. The optical paths are represented: the object beam (in red on the image) is back-scattered by the sample before interfering with the reference beam (in purple). The objective used here is simply composed of two identical lenses (f' = 100 mm) and a diaphragm.

pixels) records image-plane holograms at 500 frames/s with 200 µs integration time. Using a two-dimensional Fourier transform method, the amplitude and phase images are extracted from each frame [59]. Compared to previous designs presented in digital-holography-based elastography [52,54], the optical set-up was improved here to achieve a more compact system. With this design, the objective, here composed of a diaphragm and two identical lenses (f'=100mm), can be changed to adjust the field of view and resolution to the region of interest. In this study, a field of view (FOV) of 11×11 mm^2 is chosen with a 50 μm optical resolution and a 30 nm axial displacement sensitivity. The maximum laser power density on the sample is 8 mW/cm^2.

Two types of mechanical excitations were chosen to generate noise. A piezoelectric actuator (Cedrat Technologies, France, APA100M) was used to transmit vibrations of hundreds of nanometers in amplitude to the sample using a vibrating plate where the samples were placed. The generated noise has a determined central frequency and bandwidth. The second method of mechanical excitation consists of using fingers to tap around the sample and create low-frequency unknown noise. The proof of concept of the experimental set-up was already demonstrated for isotropic medium [52].

Since the experimental setup is only sensitive to axial displacements at the surface of the sample which is in contact with air, Rayleigh waves are considered here. A corrective coefficient should be applied to the experimental Rayleigh wave speeds $c_{Rayleigh}$ to correspond to the shear-wave's c [60]:

$$c = \frac{c_{Rayleigh}}{0.95}. \tag{10}$$

Biomedical Optics EXPRESS

2.4. Simulation and sample preparation

2.4.1. Finite Difference Simulations

In order to test the elastography approaches and algorithms, simulations were coded using Matlab. The propagation of shear-waves at the surface of a purely elastic non-absorbing medium was modeled based on the wave propagation equation with an added source term:

$$\Delta u(\overrightarrow{r},t) - \frac{1}{c^2}\frac{\partial^2 u(\overrightarrow{r},t)}{\partial t^2} = S(\overrightarrow{r},t)\,. \tag{11}$$

with $u(\overrightarrow{r},t)$ the displacement and $S(\overrightarrow{r},t)$ the source term.

As we are working with heterogeneous medium, the shear-wave speed c is space-dependent. Moreover, under the hypothesis of a transversely isotropic medium, the shear-wave speed also depends on the propagation direction. Considering those assumptions, the propagation equation is written with Cartesian coordinates in two-dimensional space and time:

$$c_x^2(x,y)\frac{\partial^2 u(x,y,t)}{\partial x^2} + c_y^2(x,y)\frac{\partial^2 u(x,y,t)}{\partial y^2} - \frac{\partial^2 u(x,y,t)}{\partial t^2} = S(x,y,t), \tag{12}$$

with $c_x(x,y)$ and $c_y(x,y)$ the speeds respectively in the direction of the x-axis and y-axis.

Transitioning to discrete coordinates, the derivatives are approximated using central finite differences for space and backward finite differences for time. The source term is composed of multiple uncorrelated point sources placed around the field of view. Each source is a noise between 300 and 900 Hz, with a central frequency of 600 Hz.

Homogeneous anisotropic media were simulated using a 100×100 pixels mesh size (100×100 μm^2 per pixel). Simulations were made at a 50 kHz sampling frequency. Then 500 frames are resampled with a sampling frequency of 500 Hz to match the camera used in experiments. The shear-wave speed along the x-axis was set at 1.5 m/s while the speed along the y-axis varies between 1 and 2 m/s, corresponding to an anisotropy ratio between 0.67 and 1.33.

2.4.2. Agarose phantoms manufacturing

As for the first tests of the experimental set-up, polymer phantoms were manufactured in order to obtain samples with controlled mechanical and optical properties in order to test the experimental set-up. Previous works in elastography have introduced samples such as anisotropic Polyvinyl Alcohol samples for magnetic resonance and ultrasound elastography [61]. We chose here to make agarose structured samples to control optical properties and for comparison with previous works [52]. Details on their fabrication are provided here.

Tissue-mimicking samples were made using agarose (A9539, Sigma–Aldrich, St. Louis, MO, USA) for mechanical properties and titanium dioxide (277370010, Acros Organics, Morris Plains, NJ, USA) for optical scattering properties. The mass concentration of agarose in the samples is 2% here. As for mechanical properties, the shear-wave speeds in such samples typically range from 1 to 10 m/s (corresponding to shear-moduli between 1 and 100 kPa), similarly to biological soft tissues [62]. The samples were 50 mL and solidified as approximately $65 \times 65 \times 15\ mm^3$ gels.

Structured samples were created to mimic the presence of fibers in tissues and create anisotropic mechanical behavior. Rice noodles were cooked for 2 minutes in boiling water, cut to a 65mm length and aligned. The agarose was then poured over the noodles. When the sample solidified, the noodles stayed at 1 to 2 mm below the samples surface. It is assumed here that the structured samples are transversely isotropic with a symmetry axis along the noodles axis. Since the mechanical properties of agarose varies depending on temperature and humidity, the samples were imaged one to three hours after being made. Time of flight measurements were performed at 1 kHz with the setup presented in [54] prior to using the noise-correlation approach presented in this paper to ensure in-plane anisotropy.

Biomedical Optics EXPRESS

3. Results

3.1. Simulation

Figure 4 displays the results of the simulations in an homogeneous media with gradually increasing anisotropy. The anisotropy ratio is defined by the ratio of the mean speeds along the x and y axis. speeds are retrieved using the trace of the Hessian matrix.

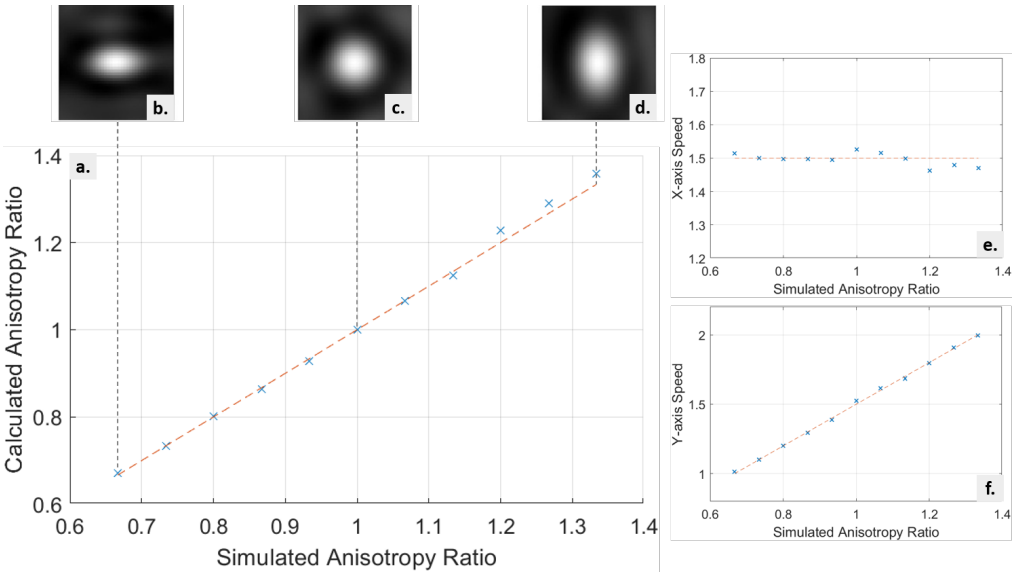

Fig. 4. Results on anisotropic media simulations. (a) is a curve representing the focal spot anisotropy using the derivative approach to noise-correlation on simulation images. Homogeneous media were simulated with a gradually increasing anisotropy ratio (between 0.67 and 1.33), represented here by the orange dash line. The simulated ratio is along the x-axis and the ratio computed from the simulated displacement movie is along the y-axis. (b), (c) and (d) are typical focal spot images displayed to illustrate these results, respectively corresponding to 0.67, 1 and 1.33 anisotropy ratio. (e) and (f) are respectively the speed values following the x-axis and the y-axis used for each anisotropy ratio. In all figures, orange dash lines represent the theoretical values and blue crosses the computed ones.

Blue crosses represent the anisotropy ratios retrieved from simulations with the noise-correlation algorithm, while the orange dashed line is the theoretically simulated anisotropy ratio. Focal spots describe visually the anisotropy in the medium. Results for the anisotropy ratios are between 0.67 and 1.36, corresponding to a error below 2%. Speed values for each anisotropy levels are plotted in Fig. 4. The error on the retrieved anisotropy level mainly comes from the error on the x-axis speed estimation and could be reduced with refined sampling. These results validate the noise correlation algorithm to evaluate the anisotropic behavior of different media.

3.2. Agarose structured samples

Experimental testing was first conducted using the structured agarose samples. Noise was created in the samples using two methods: piezoelectric actuators for high-frequency controlled noise and fingers tapping. Piezoelectric actuators between 300 and 1100 Hz with a central frequency of 700 Hz allow for the full focal spot to be retrieved. On the other hand, fingers tapping generate unknown low-frequency noise, which is closer to *in-vivo* natural noise.

As the structured sample was considered homogeneous, focal spots can be reconstructed and are displayed in Fig. 5. Results show asymmetrical focal spots. The average anisotropy ratio

Biomedical Optics EXPRESS

computed from these focal spots using their full width at half maximum provides anisotropy ratio between 0.6 and 0.7. The derivative approach was also implemented on these images (b to g). The average anisotropy ratio was of 0.7 for fingers tapping and 0.7 for piezoelectric actuators. Both approaches displayed consistent results in terms of anisotropy ratio. The difference excitation frequency between fingers tapping and controlled noise affects the focal spot size but not the retrieved anisotropy ratio.

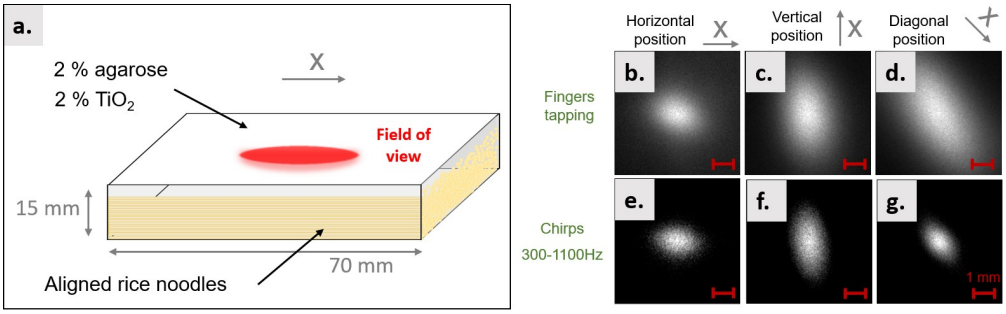

Fig. 5. Schematic of the structured agarose sample (a). Focal spots were computed using noise-correlation on one-second acquisitions at 500 Hz with two types of noise sources: fingers tapping (b, c and d) and piezoelectric actuators (e, f and g). The sample was positioned with the noodles aligned horizontally (b and e), vertically (c and f) and diagonally (d and g) in the field of view.

In order to ensure that anisotropic behavior was created from the medium's structure and not from the source's partition, the structured sample was rotated of 90 and 45 degrees (c and f and d and g respectively). It can be seen in Fig. 5 that the focal spots' major axis are indeed rotating with the sample and that their anisotropy ratio remained consistent: 0.7, 0.6 and 0.6 for e, f and g respectively. This shows that anisotropic behavior was indeed created by structuring the agarose sample. The developed experimental setup is able to characterize homogeneous anisotropic polymer samples using noise-correlation using controlled or unknown broadband sources.

A contrasted anisotropic agarose sample was then created by aligning the rice noodles along two perpendicular directions on two different sides of the sample. The field of view was centered at the interface between the two directions of alignment, as depicted in Fig. 6(a). The stiffness maps are displayed as shear-wave wavelength maps. Considering a semi-infinite homogeneous medium, these wavelengths are directly proportional to shear-wave speed ($c = \lambda f_0$) and to the medium's shear modulus (Eq. (5)). The stiffness was first assessed using the algorithm for isotropic media used in a previous publication [52] that averages the derivative along all in-plane spatial direction. The resulting image (b) shows indeed no significant contrast between both sides. However, when the stiffness is assessed separately in the x and y axes in Fig. 6(c and d) respectively, the contrast appears with an increase in shear-wave speed in the noodles' alignment direction. The anisotropy ratio f_a can be locally computed using the derivative approach of noise-correlation (f) using the ratio between the horizontal and vertical orientation axis. A red scale was used for horizontal fiber orientation ($\overrightarrow{x}$) and a blue scale for vertical fiber orientation. Additionally, the anisotropy direction (corresponding to the major axis of the local focal spot) was computed using the derivative approach (e) The average gradient is computed averaged every 30 x 30 pixels for display.

From Fig. 6(c) to 6(f), it is clearly displayed that for the same position on the image, the axis of the noodles will yield higher values of wave numbers, meaning higher stiffness. On Fig. 6(e and f), the anisotropy factor and its direction are showing locally computed anisotropy in the sample. The left part of the images mostly shows an horizontal orientation of the fibers, showing an average anisotropy ratio above 1 encoded in red. On the other hand, the right side displays

Biomedical Optics EXPRESS

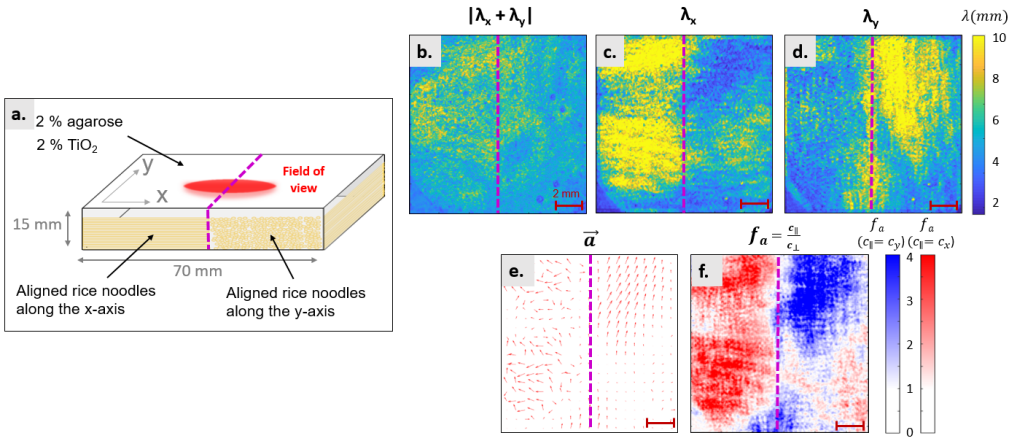

Fig. 6. Schematic of the structured contrasted agarose sample (a) and shear-wave wavelength maps (b, c and d) computed from one-second acquisitions of fingers tapping around the sample. The shear-wave speed assessments were calculated in the x-axis (c), the y-axis (d) and averaged over all direction (b). From these images the anisotropy direction $\vec{a}$ (e) and anisotropy ratio $f_a = \frac{c_\parallel}{c_\perp}$ can be locally computed. A blue scale is used when the fast axis is along the $\vec{y}$ direction and a red scale is used when the fast axis is along the $\vec{x}$ direction as defined on (a).

mostly vertical gradient on Fig. 6(e) and consequently, the anisotropy ratio is represented in blue. The lower right quadrant of the sample does appear to show less anisotropy. It is believed to be caused by a misalignment of the noodles during the sample's solidification. These results demonstrate the ability of the system to retrieve quantitative full-field mechanical anisotropic stiffness images in a contrasted structured sample.

3.3. *In-vivo test on the human forearm*

First *in-vivo* images of stiffness and anisotropy measurements are presented in this last experiment. A vibrating phone was used to create a diffuse field in the forearm. Results are displayed in Fig. 7. Two different zones were imaged: one close to the wrist (images b and d) and one closer to the elbow (images c and e). The stiffness images in the form of wavelength maps averaged over the different directions of propagation are displayed in b and c As the sample is considered homogeneous in each acquisition, the anisotropy can be displayed as a focal spot. The averaged correlation functions are presented in d and e for each zone. Shear-wave speed ratio of 1.2 and 2 were calculated for Fig. 7(d and e) respectively. These values are comparable to recently published results [20] where a ratio of 2 was found between the shear-wave speeds in perpendicular directions at the surface of a similar region of the forearm.

Biomedical Optics EXPRESS

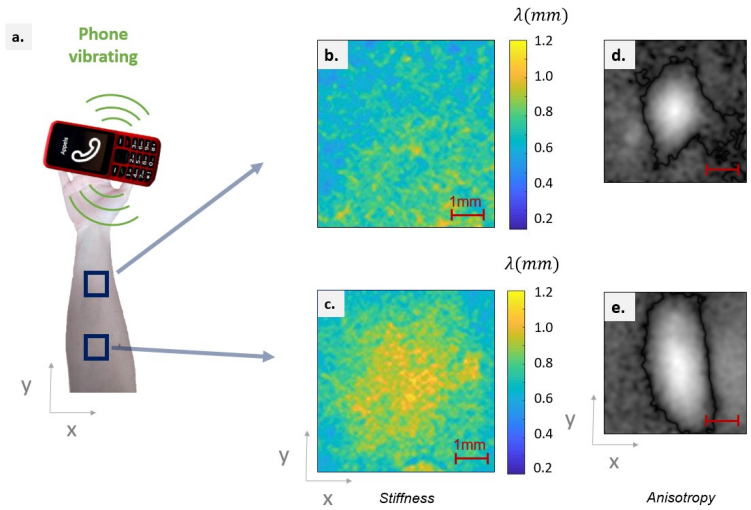

Fig. 7. Experimental data acquired on the forearm *in-vivo* using a digital holography set-up. A vibrating phone was used as the source of mechanical vibrations. Two different zones were imaged as displayed in a. The first one is closer to the wrist (b and d) and the other closer to the elbow (c and e). The estimated shear-wave wavelength maps are presented in b and c The corresponding average correlation function from the same acquisitions is presented in (d) and (e).

4. Discussion and conclusion

In this study, quantitative full-field anisotropic stiffness images were performed successfully using a digital-holography setup with a noise-correlation approach. Finite difference simulations have been performed for homogeneous anisotropic media for validation. Experimental results are also presented on polymer structured sample, displaying the potential for this set-up to retrieve mechanical anisotropy in a sample using a noise-correlation-based approach. Promising preliminary results on the human forearm *in-vivo* are also displayed, showing the adaptability of the portable non-contact optical set-up for future clinical use. Additionally, our approach eliminates the need for a controlled mechanical source, enabling full-field stiffness and anisotropy imaging within seconds without sample rotation. Although further experiments such as a repeatability study and additional *ex-vivo* testing would be crucial to move towards clinical application, this study highlights the robustness and versatility of the presented method.

In this study, it was assumed that the sample was incompressible and transversely isotropic with the fiber's direction in the plane of imaging. If it is not the case and the fibers in the sample are oriented in a direction which is not parallel to the imaging plane, the anisotropy ratio of the sample will be underestimated. In order to avoid this bias, a 3D full-field imaging system could be implemented such as a full-field OCT [63–65]. Other bias common to most elastography approaches should also be considered such as viscoelasticity or the finite dimensions of the sample, the presence of guided waves or pre-stress [66]. In particular, the presence of guided waves could cause the noise-correlation to underestimate the shear-wave speed as guided waves have lower propagation speeds in biological tissues compared to shear-waves.

In this paper, in order to retrieve the medium anisotropy ratio, it is assumed that the noise energy partition is isotropic. This is the main assumption for performing noise-correlation in scattering media [67]. Yet, as shown previously [54], stiffness measurements can be biased if the condition of source equipartition is not respected. This influence is especially significant when providing anisotropy measurements as displayed in recent work in seismology [68]. Correlations

Biomedical Optics EXPRESS

shifted in time and space could notably provide valuable information on energy partition. Further investigations could be conducted to investigate the possibility to detect or correct biases due to an anisotropic energy distribution of noise sources as it is likely to be the case in *in-vivo* tissues.

As this paper presents anisotropy images, the question of the resolution of the system is a significant issue. The optical resolution on the set-up shown in this study can be easily determined theoretically and experimentally. However, the elastography resolution is more difficult to establish as it depends on the system's signal to noise ratio [69]. Under the assumption of isotropic mechanical properties of the samples, the stiffness measurements can be averaged over different directions at each point, which increases signal. However, in the presented approaches for anisotropy imaging, each orientation is computed separately, which decreases signal and decreases resolution compared to a previous study [52].

This paper presents a new approach for anisotropy imaging allowing for full-field anisotropy imaging without the need to rotate the sample. Contrary to previous approaches, a single acquisition is sufficient to provide mechanical anisotropy contrast images. A real-time implementation can be achieved using a GPU, which is very promising for clinical translation. The optical system is also adaptable to different sizes of field of view, which could be useful in further studies to investigate anisotropy at different scales.

Funding. Agence Nationale de la Recherche (ANR-11-INBS-0006, ANR-21-CE19-0018-01); Institut des sciences de l'ingénierie et des systèmes (PEPS - La Mecanique du Futur, 2021).

Disclosures. The authors declare no conflicts of interest.

Data availability. Data underlying the results presented in this paper are not publicly available at this time but may be obtained from the authors upon reasonable request.

References

1. T. Krouskop, D. Dougherty, F. Vinson, *et al.*, "A pulsed doppler ultrasonic system for making noninvasive measurements of the mechanical properties of soft tissue," J Rehabil Res Dev **24**(2), 1–8 (1987).
2. J. Ophir, I. Céspedes, H. Ponnekanti, *et al.*, "Elastography: A quantitative method for imaging the elasticity of biological tissues," Ultrason. Imaging **13**(2), 111–134 (1991).
3. C. J. Lewa, "Magnetic resonance imaging in the presence of mechanical waves," Spectrosc. Lett. **24**(1), 55–67 (1991).
4. R. Muthupillai, D. J. Lomas, P. J. Rossman, *et al.*, "Magnetic resonance elastography by direct visualization of propagating acoustic strain waves," Science **269**(5232), 1854–1857 (1995).
5. J. M. Schmitt, "OCT elastography: imaging microscopic deformation and strain of tissue," Opt. Express **3**(6), 199 (1998).
6. B. F. Kennedy, P. Wijesinghe, and D. D. Sampson, "The emergence of optical elastography in biomedicine," Nat. Photonics **11**(4), 215–221 (2017).
7. S. Wang and K. V. Larin, "Shear wave imaging optical coherence tomography (swi-oct) for ocular tissue biomechanics," Opt. Lett. **39**(1), 41–44 (2014).
8. C. Liu, A. Schill, C. Wu, *et al.*, "Non-contact single shot elastography using line field low coherence holography," Biomed. Opt. Express **7**(8), 3021–3031 (2016).
9. S. Song, N. Le, Z. Huang, *et al.*, "Quantitative shear-wave optical coherence elastography with a programmable phased array ultrasound as the wave source," Opt. Lett. **40**(21), 5007–5010 (2015).
10. J.-L. Gennisson, S. Catheline, S. Chaffai, *et al.*, "Transient elastography in anisotropic medium: Application to the measurement of slow and fast shear wave speeds in muscles," J. Acoust. Soc. Am. **114**(1), 536–541 (2003).
11. J. L. Gennisson, C. Cornu, S. Catheline, *et al.*, "Human muscle hardness assessment during incremental isometric contraction using transient elastography," J. biomechanics **38**(7), 1543–1550 (2005).
12. I. Sack, J. Bernarding, and J. Braun, "Analysis of wave patterns in mr elastography of skeletal muscle using coupled harmonic oscillator simulations," Magn. Reson. Imaging **20**(1), 95–104 (2002).
13. S. Papazoglou, J. Rump, J. Braun, *et al.*, "Shear wave group velocity inversion in mr elastography of human skeletal muscle," Magn. Reson. Med. An Off. J. Int. Soc. for Magn. Reson. Med. **56**(3), 489–497 (2006).
14. S. Leong, J. Wong, M. Md Shah, *et al.*, "Stiffness and anisotropy effect on shear wave elastography: A phantom and in vivo renal study," Ultrasound Med. Biol. **46**(1), 34–45 (2020).
15. J. Schmidt, D. Tweten, A. Badachhape, *et al.*, "Measurement of anisotropic mechanical properties in porcine brain white matter ex vivo using magnetic resonance elastography," J. Mech. Behav. Biomed. Mater. **79**, 30–37 (2018).
16. P. Kalra, B. Raterman, X. Mo, *et al.*, "Magnetic resonance elastography of brain: Comparison between anisotropic and isotropic stiffness and its correlation to age," Magn. Reson. Med. **82**(2), 671–679 (2019).
17. M. McGarry, E. Van Houten, D. Sowinski, *et al.*, "Mapping heterogenous anisotropic tissue mechanical properties with transverse isotropic nonlinear inversion mr elastography," Med. Image Anal. **78**, 102432 (2022).

Biomedical Optics EXPRESS

18. R. Sinkus, M. Tanter, T. Xydeas, *et al.*, "Viscoelastic shear properties of in vivo breast lesions measured by mr elastography," Magn. Reson. Imaging **23**(2), 159–165 (2005).
19. S. Gahagnon, Y. Mofid, J. Gwendal, *et al.*, "Skin anisotropy in vivo and initial natural stress effect: A quantitative study using high-frequency static elastography," J. biomechanics **45**(16), 2860–2865 (2012).
20. M. A. Kirby, P. Tang, H.-C. Liou, *et al.*, "Probing elastic anisotropy of human skin in vivo with light using non-contact acoustic micro-tapping oce and polarization sensitive oct," Sci. Rep. **12**(1), 3963 (2022).
21. M. Singh, J. Li, Z. Han, *et al.*, "Investigating elastic anisotropy of the porcine cornea as a function of intraocular pressure with optical coherence elastography," J. Refract. Surg. **32**(8), 562–567 (2016).
22. M. A. Kirby, J. J. Pitre Jr, H.-C. Liou, *et al.*, "Delineating corneal elastic anisotropy in a porcine model using noncontact oct elastography and ex vivo mechanical tests," Ophthalmol. Sci. **1**(4), 100058 (2021).
23. B. Babaei, D. Fovargue, R. A. Lloyd, *et al.*, "Magnetic resonance elastography reconstruction for anisotropic tissues," Med. Image Anal. **74**, 102212 (2021).
24. D. P. Pioletti and L. R. Rakotomanana, "Non-linear viscoelastic laws for soft biological tissues," Eur. J. Mech. **19**(5), 749–759 (2000).
25. C. Whitford, N. V. Movchan, H. Studer, *et al.*, "A viscoelastic anisotropic hyperelastic constitutive model of the human cornea," Biomech. Model. Mechanobiol. **17**(1), 19–29 (2018).
26. S. Delp and S. Blemker, "Three-dimensional representation of complex muscle architectures and geometries," Ann. Biomed. Eng. **33**(5), 661–673 (2005).
27. S. F. Levinson, "Ultrasound propagation in anisotropic soft tissues: the application of linear elastic theory," J. biomechanics **20**(3), 251–260 (1987).
28. P. L. Kuo, P. C. Li, and M. L. Li, "Elastic properties of tendon measured by two different approaches," Ultrasound Med. Biol. **27**(9), 1275–1284 (2001).
29. J.-L. Gennisson, N. Grenier, C. Combe, *et al.*, "Supersonic shear wave elastography of in-vivo pig kidney: Influence of blood pressure, urinary pressure and tissue anisotropy," Ultrasound Med. Biol. **38**(9), 1559–1567 (2012).
30. K. Skerl, S. Vinnicombe, K. Thomson, *et al.*, "Anisotropy of solid breast lesions in 2d shear wave elastography is an indicator of malignancy," Acad. radiology **23**(1), 53–61 (2016).
31. Y.-L. Chen, Y. Gao, C. Chang, *et al.*, "Ultrasound shear wave elastography of breast lesions: Correlation of anisotropy with clinical and histopathological findings," Cancer imaging : official publication Int. Cancer Imaging Soc. **18**(1), 11 (2018).
32. M. Correia, T. Deffieux, S. Chatelin, *et al.*, "3d elastic tensor imaging in weakly transversely isotropic soft tissues," Phys. Med. Biol. **63**(15), 155005 (2018).
33. X. Leng, R. Japaer, H. Zhang, *et al.*, "Relationship of shear wave elastography anisotropy with tumor stem cells and epithelial-mesenchymal transition in breast cancer," BMC Med. Imaging **21**(1), 171 (2021).
34. O. Pedreira, M. Correia, S. Chatelin, *et al.*, "Smart ultrasound device for non-invasive real-time myocardial stiffness quantification of the human heart," IEEE Trans. Biomed. Eng. **69**(1), 42–52 (2022).
35. S. Lee, L. Y. Eun, J. Y. Hwang, *et al.*, "New metric to evaluate cardiac anisotropic mechanics by directional high-frequency ultrasound-based transverse wave elastography," IEEE Trans. Ultrason., Ferroelect., Freq. Contr. **70**(7), 653–667 (2023).
36. M. Green, J. Geng, E. Qin, *et al.*, "Measuring anisotropic muscle stiffness properties using elastography," NMR Biomed. **26**(11), 1387–1394 (2013).
37. E. Qin, R. Sinkus, J. Geng, *et al.*, "Combining mr elastography and diffusion tensor imaging for the assessment of anisotropic mechanical properties: A phantom study," J. magnetic resonance imaging : JMRI **37**(1), 217–226 (2013).
38. S. Chatelin, I. Charpentier, N. Corbin, *et al.*, "An automatic differentiation-based gradient method for inversion of the shear wave equation in magnetic resonance elastography: specific application in fibrous soft tissues," Phys. Med. Biol. **61**(13), 5000–5019 (2016).
39. O. Pedreira, M. Correia, S. Chatelin, *et al.*, "Smart ultrasound device for non-invasive real-time myocardial stiffness quantification of the human heart," IEEE Transactions on Biomedical Engineering (2022).
40. H. H. P. Ngo, R. J. Andrade, J. Lancelot, *et al.*, "Unravelling anisotropic nonlinear shear elasticity in muscles: towards a non-invasive assessment of stress in living organisms," J. Mech. Behav. Biomed. Mater. **150**, 106325 (2024).
41. A. Athanasiou, A. Tardivon, M. Tanter, *et al.*, "Breast lesions: quantitative elastography with supersonic shear imaging—preliminary results," Radiology **256**(1), 297–303 (2010).
42. E. C. Qin, L. Jugé, S. A. Lambert, *et al.*, "In vivo anisotropic mechanical properties of dystrophic skeletal muscles measured by anisotropic MR elastographic imaging: the MDX mouse model of muscular dystrophy," Radiology **273**(3), 726–735 (2014).
43. C. Galban, S. Maderwald, B. Herrmann, *et al.*, "Measuring skeletal muscle elasticity in patients with hypogonadism by mr elastography," in Proceedings of the 13th Annual Meeting of ISMRM, (2005).
44. C. Galban, S. Maderwald, H. Eggebrecht, *et al.*, "Monitoring the effects of chronic obstructive pulmonary disease on muscle elasticity by mr elastography," in Proceeding of the 13th Annual Meeting of ISMRM, (2005), p. 2015.
45. P. Grasland-Mongrain, A. Zorgani, S. Nakagawa, *et al.*, "Ultrafast imaging of cell elasticity with optical microelastography," Proc. Natl. Acad. Sci. **115**(5), 861–866 (2018).
46. F. Zvietcovich, M. Singh, Y. S. Ambekar, *et al.*, "Micro air-pulse spatial deformation spreading characterizes degree of anisotropy in tissues," IEEE J. Sel. Top. Quantum Electron. **27**(4), 1–10 (2021).

Biomedical Optics EXPRESS

47. G. Regnault, M. A. Kirby, R. K. Wang, *et al.*, "Possible depth-resolved reconstruction of shear moduli in the cornea following collagen crosslinking (CXL) with optical coherence tomography and elastography," Biomed. Opt. Express **14**(9), 5005–5021 (2023).
48. F. Zvietcovich, P. Pongchalee, P. Meemon, *et al.*, "Reverberant 3d optical coherence elastography maps the elasticity of individual corneal layers," Nat. Commun. **10**(1), 4895 (2019).
49. L. Ambrozinski, S. Song, S. J. Yoon, *et al.*, "Acoustic micro-tapping for non-contact 4d imaging of tissue elasticity," Sci. Rep. **6**(1), 38967 (2016).
50. A. Nair, M. Singh, S. R. Aglyamov, *et al.*, "Heartbeat OCE: corneal biomechanical response to simulated heartbeat pulsation measured by optical coherence elastography," J. Biomed. Opt. **25**(05), 1–9 (2020).
51. T.-M. Nguyen, A. Zorgani, M. Lescanne, *et al.*, "Diffuse shear wave imaging: toward passive elastography using low-frame rate spectral-domain optical coherence tomography," J. Biomed. Opt. **21**(12), 126013 (2016).
52. A. Marmin, S. Catheline, and A. Nahas, "Full-field passive elastography using digital holography," Opt. Lett. **45**(11), 2965–2968 (2020).
53. D. Royer and E. Dieulesaint, *Elastic waves in solids I: Free and guided propagation* (Springer Science & Business Media, 1999).
54. A. Marmin, G. Laloy-Borgna, S. Facca, *et al.*, "Time-of-flight and noise-correlation-inspired algorithms for full-field shear-wave elastography using digital holography," J. Biomed. Opt. **26**(08), 1–15 (2021).
55. J. Brum, N. Benech, T. Gallot, *et al.*, "Shear wave elastography based on noise correlation and time reversal," Front. Phys. **9**, 617445 (2021).
56. S. Chatelin, J.-L. Gennisson, M. Bernal, *et al.*, "Modelling the impulse diffraction field of shear waves in transverse isotropic viscoelastic medium," Phys. Med. Biol. **60**(9), 3639–3654 (2015).
57. V. Vavryčuk, "Asymptotic green's function in homogeneous anisotropic viscoelastic media," Proc. R. Soc. A **463**(2086), 2689–2707 (2007).
58. S. Catheline, R. Souchon, M. Rupin, *et al.*, "Tomography from diffuse waves: Passive shear wave imaging using low frame rate scanners," Appl. Phys. Lett. **103**(1), 014101 (2013).
59. N. Verrier and M. Atlan, "Off-axis digital hologram reconstruction: some practical considerations," Appl. Opt. **50**(34), H136–H146 (2011).
60. I. A. Viktorov, "Rayleigh and lamb waves: Physical theory and applications," Plenum Press p. 3 (1967).
61. S. Chatelin, M. Bernal, T. Deffieux, *et al.*, "Anisotropic polyvinyl alcohol hydrogel phantom for shear wave elastography in fibrous biological soft tissue: a multimodality characterization," Phys. Med. Biol. **59**(22), 6923–6940 (2014).
62. A. Sarvazyan, M. Urban, and J. F. Greenleaf, "Acoustic waves in medical imaging and diagnostics," Ultrasound Med. Biol. **39**(7), 1133–1146 (2013).
63. E. M. Seromenho, A. Marmin, S. Facca, *et al.*, "Single-shot off-axis full-field optical coherence tomography," Appl. Phys. Lett. **121**(11), 1 (2022).
64. A. Nahas, M. Bauer, S. Roux, *et al.*, "3D static elastography at the micrometer scale using Full Field OCT," Biomed. Opt. Express **4**(10), 2138–2149 (2013).
65. A. Nahas, M. Tanter, T.-M. Nguyen, *et al.*, "From supersonic shear wave imaging to full-field optical coherence shear wave elastography," J. Biomed. Opt. **18**(12), 121514 (2013).
66. J. Crutison, M. Sun, and T. J. Royston, "The combined importance of finite dimensions, anisotropy, and pre-stress in acoustoelastography," J. Acoust. Soc. Am. **151**(4), 2403–2413 (2022).
67. A. Derode, E. Larose, M. Tanter, *et al.*, "Recovering the green's function from field-field correlations in an open scattering medium (l)," J. Acoust. Soc. Am. **113**(6), 2973–2976 (2003).
68. B. Giammarinaro, C. Tsarsitalidou, G. Hillers, *et al.*, "Seismic surface wave focal spot imaging: numerical resolution experiments," Geophys. J. Int. **232**(1), 201–222 (2022).
69. C. Zemzemi, A. Zorgani, L. Daunizeau, *et al.*, "Super-resolution limit of shear-wave elastography," EPL **129**(3), 34002 (2020).